Corrosion Behavior of Strained Rebar in Simulated Concrete Pore Solution

Prasanna Kumar Behera, Sudhir Misra, and K. Mondal

Parts of reinforcing steel bar (rebar) used in concrete are subjected to high levels of plastic strain due to various operations during construction. This work presents the corrosion behavior of pre-strained rebars in simulated concrete pore solution, both in the presence and in the absence of chlorides. Results obtained from the electrochemical tests (EIS and cyclic polarization) in chloride-free pore solutions have indicated the formation of more protective passive films in the strained steels. However, when contaminated with chlorides, the strained steels have exhibited higher corrosion susceptibility due to the changes in the surface condition, microstructure and dislocation density.

1. Introduction

Corrosion of reinforcing steel bars (rebars) in concrete is a serious durability issue in reinforced concrete (RC) structures, and this has attracted both corrosion and structural engineers. Rebar inside concrete remains passive due to the formation of a protective oxide film on its surface (Ref 1, 2). The formation and the stability of the passive film are influenced by several factors, such as pH of the pore solution, composition of steel and concrete, oxygen availability and the presence of external agents, like chlorides and carbon dioxide (Ref 3-6). It is widely known that chloride-induced rebar corrosion occurs when the chloride ions, accumulated at the steel–concrete interface, cause the localized breakdown of the passive film (Ref 7-9).

Examining the corrosion tendency of rebar in a given environment requires the quantification of the electrochemical parameters of the double layer formed at the interface. As far as corrosion characteristics of rebar are concerned, studying them in mortar/concrete would always be a holistic approach, as they represent the actual service conditions more closely. However, in such studies, several other considerations, such as the effective exposed area of test specimens, tendency to form crevice and the relative effects of micro- and macrocells at the steel–concrete interface, could intervene in the experimental approach (Ref 9). These complex and combined effects on the corrosion damage would take years for realization. In addition, the individual influence of these parameters on the corrosion is always a challenge. In order to avoid these effects, researchers have often studied the corrosion characteristics of rebar in simulated concrete pore solutions (Ref 3-15), which have

similar chemical environment as that of the cementitious system. Several stoichiometric combinations of NaOH, KOH, $Ca(OH)_2$ and/or gypsum have been reported as pore solutions in the literature (Ref 3-15). However, their effectiveness to represent the mortar/concrete environment is based on the pH of the test electrolyte (normal range 12.4 to 13.4) and the semiconducting behavior of the passive film formed on the surface of the rebar (Ref 11). Furthermore, it has also been reported that for the solutions having higher pH, higher levels of chlorides are needed to cause a significant damage to the passive layer formed on carbon steels (Ref 14, 15).

Another important factor, which influences the passive layer formation on the rebar and the subsequent pitting attack due to chlorides, is the surface condition of the rebar (Ref 15). Figueira et al. (Ref 15) have studied the effect of surface finish on the chloride threshold to initiate corrosion of rebar and reported that pre-oxidized steel specimens have higher chloride threshold than polished specimens. Therefore, to achieve a meaningful understanding on the effect of a given parameter on the corrosion tendency of rebar, it is crucial to consider the factors, such as surface condition, pH of the test electrolyte and the amount of chlorides to study the depassivation behavior.

Fundamental aspects, addressed in the past related to the rebar corrosion, include its mechanism (Ref 1, 16, 17), chloride threshold (Ref 7, 8, 15, 18, 19) and its subsequent aftermaths on the RC member, such as crack initiation and propagation in concrete (Ref 20-23). A key aspect, which is worth addressing, is the stress-accompanied rebar corrosion in concrete. Studies related to this aspect have investigated the flexural behavior of the loaded RC members subjected to rebar corrosion and have reported higher deflections and crack widths as compared to the unloaded members (Ref 24-30). In an attempt to understand the electrochemical behavior of the rebar inside the loaded RC members, Aveldaño and Ortega (Ref 31) have examined the corrosion potential of rebar and reported greater active potential in the compressed reinforcement than the tensioned one. Feng et al. (Ref 32) have examined the influence of stress on the passivation behavior of steel bars in simulated concrete pore solution and reported that the passivation ability decreases due to the presence of sustained external load. In another study, Feng et al. (Ref 33) have studied the impact of both the compressive and tensile stresses on the corrosion behavior of

Prasanna Kumar Behera and Sudhir Misra, Department of Civil Engineering, Indian Institute of Technology, Kanpur, Kanpur 208016, India; and K. Mondal, Department of Materials Science and Engineering, Indian Institute of Technology, Kanpur, Kanpur 208016, India. Contact e-mail: kallol@iitk.ac.in.

rebar embedded in mortar and immersed in 3% NaCl solution with the help of linear polarization and impedance spectroscopy. They have reported an increase in the corrosion activity of the rebar due to the formation of microcracks in the mortar in the presence of an external load.

In one of their recent works, Li and Wu (Ref 34) have studied the degree of corrosion of rebar under varying tensions and reported that the extent of corrosion increases in the stressed rebar. Shi et al. (Ref 35) have investigated the corrosion performance of rebar in concrete under the simultaneous action of flexural load and chloride attack. They have found that the chloride attack on the steel in the tensile portion of the concrete is considerably severe. The authors have attributed this behavior to the defects formed at the concrete–steel interface during the casting (Ref 34). Li et al. (Ref 36) have reported an increase in the rate of corrosion at higher stress levels in high-strength steel strands of pre-stressed concrete specimens. Interestingly, Zhang and Poursaee (Ref 11) have reported that corrosion tendency of steels under tension in chloride-free simulated concrete pore solution is lower than that of the compressed and unstressed ones. However, in the presence of chlorides, an opposite behavior in the tensioned steel has been observed by them in pore solution. Furthermore, they have also reported that the stress in steel is more crucial than the presence of the passive layer in deciding the corrosion behavior of steel in chloride-contaminated pore solutions.

A close examination of the published research (Ref 24-36) relevant to the stress-accompanied rebar corrosion clearly shows that the rebar has been subjected to stresses and strains within the elastic region, leading to an increase in its corrosion susceptibility. One important aspect that has received scant attention is the corrosion behavior of rebar, subjected to pre-induced plastic strains. This is, particularly, of concern to civil engineers because apart from the elastic strains arising in case of usual structural loads, the rebar inside concrete could be subjected to very high levels of plastic strain due to various structural operations at construction sites. For example, rebars are bent into various forms for construction purposes (example: bent-up bars, stirrups or joints), resulting in the generation of huge amount of plastic strains at the bends (Ref 37). In the close vicinity of a cracked RC beam, the steel would be subjected to significant levels of plastic strain (Ref 38).

The mechanical properties of steel subjected to the combined action of plastic deformation and corrosion have been examined by Apostolopoulos and Michalopoulos (Ref 39). They have reported a remarkable decrease in the strength and ductility of the strained steels due to corrosion. Feng et al. (Ref 40) have studied the passivation and repassivation behavior of carbon steel in concrete pore solution, which has been subjected to an external load using a three-point loading mechanism, and reported that there would be severe damage to the passive films at higher levels of external load. The poor repassivation behavior of the steels in concrete pore solution after unloading has also been observed by them (Ref 40). A closer look at the results reported in the work of Feng et al. (Ref 40) clearly indicates that the electrochemical measurements on the passivated steels mostly depend on the extent of microcracks formed in the passive films. In an another study, the influence of pre-induced plastic strain on the passive behavior of carbon steel has been examined by Feng et al. (Ref 41) and reported that passive films formed on strained steels tend to be unstable due to the changes occurring in their donor density and Fe^{3+}/Fe^{2+} ratio.

However, unlike the elastic strains, which are induced due to external load after casting the RC member, the plastic strains in the steels at the bends are induced prior to embedding them in concrete. In actual situation, depending on the angle of the bend and the diameter of the mandrel used, different levels of plastic strain could be induced in its tensile portion. If closely observed near the location of the bend (Fig. 1(a), a trial experiment in the present work), mill-scale, a thin adherent oxide layer present on the surface of any commercial rebar (Ref 12, 42), is damaged due to the plastic deformation, whereas the scale on the unstrained portion is not damaged. This would lead to the surface dissimilarity at various portions on the rebar, which are to be taken into account for a more meaningful understanding on their corrosion behavior.

Unlike the usual elastic strains in the steel because of the external loading on the RC member, plastic strains could result in a significant change in the steel both at macroscopic and at microscopic levels. It is worth mentioning that the previous studies (Ref 43-45), reporting the microstructural differences in carbon steel arising on account of strain, are related to the warm deformation of steel, which happens before the final product is made. However, at construction sites, the plastic strains are induced in the final product (rebar) itself. Therefore, the associated change in the microstructure could be different, and a critical examination of such changes has never been studied.

Therefore, understanding these microstructural differences and their impact on the corrosion behavior of the strained steels is crucial in order to highlight the special care and attention required at bends and hooks of a reinforcement. To the best of the current authors' knowledge, limited numbers of studies related to the corrosion behavior of rebar having pre-induced plastic strains in simulated pore solution have been carried out till date. Therefore, with an intention to provide a fresh perspective to the problem, the present research focuses on examining the corrosion behavior of a rebar having different levels of pre-induced plastic strains from an electrochemical viewpoint. Various measurements on the strained rebar specimens, such as open-circuit potentials, electrochemical impedance spectroscopy (EIS) and cyclic polarization (CP) tests, have been performed in both chloride-free and chloride-contaminated concrete pore solutions. The paper also presents the nature of the corrosion products formed on the strained steel surface at the end of cyclic polarization tests in chloride-contaminated pore solution.

2. Experimental Details

2.1 Specimen Preparation and Metallography

Plain reinforcing steel bars of 20 mm diameter and having composition 98.9% Fe, 0.14% C, 0.15% Si, 0.38% Mn, 0.05% P, 0.05% S, 0.08% Cr, 0.05% Ni, 0.096% Cu, 0.002% V (all are in weight%) and other elements in traces, were used to prepare the specimens for testing. The bars were conforming to IS 432 (part-1):1982 (Ref 46). The typical stress–strain behavior of the steel bar subjected to tensile loading in Tinius Olsen Model 2000SL as per IS 1608:2005 (Ref 47) is shown in Fig. 1(b). It could be clearly seen that the yield point was obtained at 0.2% strain level, and the corresponding yield strength was 335 ± 3 MPa. Ultimate strength of the steel was 520 ± 5 MPa. Based on the stress–strain response of the steel,
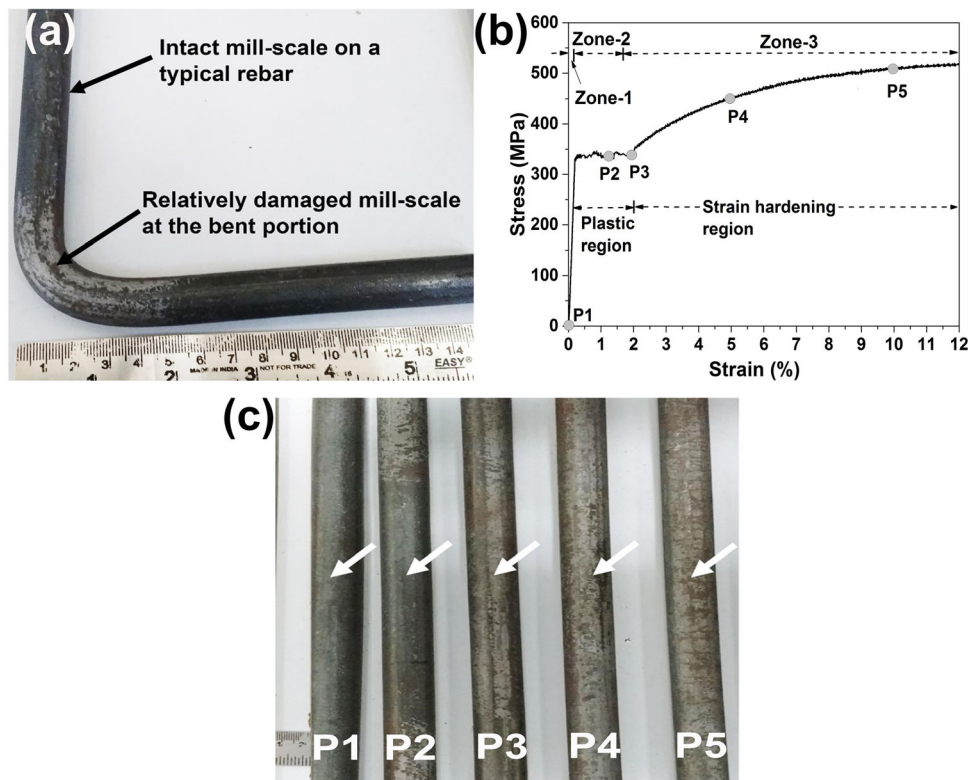
Fig. 1 (a) A typical 90° bend of a rebar. (b) Stress–strain behavior of the rebar along with the details of the notations followed for various levels of pre-tensioning. (c) Unstrained (P1) and strained rebars (P2-P5) with the arrow showing the portion under study

four different levels of tensioning apart from the unstrained (control) as shown in Fig. 1(b) were employed to incorporate different levels of plastic strain. After tensioning the 600-mm-long steel bars to various levels in a Universal Testing Machine (Tinius Olsen Model 2000SL) at a loading rate of 0.0025 s^{-1}, the bars were unloaded and the final diameters were measured using a highly precise Vernier calipers. While P1 was not strained for reference, the specimens, P2-P5, were pre-strained to a level of 1%, 2.2%, 5.0% and 10.0%, respectively, and were pertaining to various zones in the stress–strain curve as shown in Fig. 1(b). The rebars used in the study are shown in Fig. 1(c). For further microscopic observations and electro-chemical testing, test specimens of 15 mm thickness were prepared from the central portions of the rebars, and thus, it was ensured that the end effects arising because of the gripping in the testing machine were eliminated.

To reveal the change in the microstructure of the specimen on account of pre-straining, the cross sections were polished up to 1200 grit using SiC emery papers. Thereafter, the specimens were cloth-polished using 0.3-μm alumina suspension and etched using 3% Nital. Microscopic observations of the specimens were carried out using FE-SEM (Nova NanoSEM 450). The changes in the cementite lamellae of the specimens arising on the account of tensioning were carefully examined. Few un-etched specimens were examined in FE-SEM (Nova NanoSEM 450) to observe the stretch marks on the surface after polishing them thoroughly using colloidal silica suspension. It could be noted that the 600-mm-long steel bars used in the present investigation were prepared from a single 12-m-long rebar, and therefore, the change in their microstructure and electrochemical behavior of the specimens can be attributed to the level of pre-induced plastic strains in them.

For electrochemical testing, the electrical connections of the specimens were done by soldering strong copper wires on their cross sections after ultrasonically cleaning them using acetone. The cross sections of the specimens were coated using standard lacquer such that only their curved surfaces are exposed to the electrolytes. Sufficient care was exercised while coating the lacquer to eliminate the possibility of crevice formation at the junctions.

2.2 Testing and Characterization

Electrochemical measurements were taken in both simulated chloride-free (SCPS) and chloride-contaminated (SCPS + Cl$^-$) pore solutions. The simulated concrete pore solution comprised of 0.1 M NaOH, 0.3 M KOH, 0.03 M Ca(OH)$_2$ and 0.002 M gypsum (pH $\simeq$ 12.6). The chloride-contaminated pore solution was prepared by adding the 5% NaCl (by weight) along with 0.1 M NaOH, 0.3 M KOH, 0.03 M Ca(OH)$_2$ and 0.002 M gypsum. The pH of the solution after the addition of NaCl was 12.5. The solutions were prepared using analytical grade reagents. Initially, all the specimens were immersed for 7 days in SCPS without any chloride addition. This was particularly done to mimic the actual situation in which the stabilization of potential on the steel embedded in concrete occurs within 3-4 days (Ref 2, 48). On the 8th day, some of the specimens were tested in SCPS, and the remaining were tested in SCPS + Cl$^-$. To ensure the reproducibility, each test was repeated three times on different specimens.

The tests were carried out using an electrochemical work-station (Parstat 2263) at room temperature. A typical round-bottom cell equipped with three-electrode setup was used to obtain the measurements. The specimens obtained from the

rebars and a platinum wire mesh of larger area were used as working and counter electrodes, respectively. Saturated calomel electrode ($E° = +0.242$ V with respect to standard hydrogen electrode) was used as reference electrode. After the initial 1-h stabilization of potentials (open-circuit potential) in the test electrolyte, electrochemical impedance spectroscopy (EIS) and cyclic polarization (CP) tests were carried out sequentially. The specimens were subjected to AC perturbation of ± 10 mV with respect to the OCP to obtain the charge-transfer resistance of the specimens. The frequency was swept from 100 kHz to 10 mHz. The results of EIS were modeled and analyzed using an appropriate equivalent electrical circuit (EEC) model available in ZsimpWin software (Princeton Applied Research, USA). The forward scan in all the CP measurements was performed from -250 to 1000 mV with respect to OCP, which was followed by a reverse scan to reach -250 mV from OCP. A scan rate of 0.5 mV/s was employed in all the tests.

Various parameters, such as corrosion potential (E_{corr}), corrosion current density (i_{corr}), passivation range (given by either ($E_{oe} - E_p$) or ($E_b - E_p$) as the case may be, where E_{oe}, E_p and E_b denote the oxygen evolution potential, passivation potential and breakdown potential, respectively), the maximum anodic current density in the forward scan (i_{fm}), the potential of anodic–cathodic transition (E_{act}) and the passive current densities in the forward scan (i_{pf}) and backward scan (i_{pb}), were extracted from the CP curve. E_b was noticed in the chloride-contaminated pore solution. In addition, the extent of damage (DF, i.e., damage factor) occurred on the specimen because the high anodic polarization was calculated using Eq. 1, which could be considered to be a representative measure of the damage, especially in case of pitting attack. If the DF is less than one, the surface is in state of a passive condition or pit closure. On the other hand, a damaged surface, which indicates no pit closure, has its DF more than one. The higher the DF, the higher would be the rate of further damage.

$$\text{DF} = \frac{\text{Passive current density in the backward scan}(i_{pb})}{\text{Passive current density in the forward scan}(i_{pf})}$$

(Eq 1)

At the end of the CP tests in chloride-contaminated pore solution, the curved surface of each specimen was observed in optical microscope (Zeiss Axio Imager M1m). To aid this microscopic examination, the surface of the corroded specimen was polished using an ultra-fine emery paper (Grit 800). This had not only assisted in removing the rust carefully, but also helped in avoiding any further unwanted damage to its surface.

In addition, the corrosion products formed on the steels at the end of the CP tests in chloride-contaminated pore solution were characterized using FTIR and Raman spectroscopy. It could be worth mentioning that the spectroscopic examination of the corrosion products was carried out only in case of the CP tests performed in SCPS + Cl$^-$ in which the DF of the surface was found out to be more than one. The FTIR spectra were recorded in a range of 400-4000 cm^{-1} using a standard KBr beam splitter and rock-solid interferometer in PerkinElmer Spectrum Two FTIR spectrometer. The Raman spectra, on the other hand, were obtained using Nd:YAG laser at 532 nm in STR Raman having TE-PMT detector. Identification of a particular phase in the rust sample has been achieved by comparing the wave numbers at the dips in the FTIR spectra with their characteristic values (Ref 49) and the peaks in the Raman spectra with their distinctive shifts (Ref 49). After the qualitative characterization of the corrosion products, efforts were made to quantify the relative presence of various phases by deconvolution of the FTIR spectra at their respective dips. The deconvolution of the spectra was done with respect to a baseline formed by joining the apexes of the spectra from which the dips had originated. The α/γ^* ratio of the rust indicating its protectiveness (Ref 50) was calculated using Eq. 2.

$$\frac{\alpha}{\gamma^*} = \frac{\text{Proportion of } \alpha-FeOOH}{\text{Sum of proportions of } \gamma-FeOOH, \ \beta-FeOOH \text{ and } Fe_3O_4}$$

(Eq 2)

3. Results and Discussion

3.1 Metallographic Observations

Macroscopic observation of the strained rebars has clearly confirmed the change in their surface appearance (Fig. 1c). Mill-scale, which is present throughout the length of the unstrained rebar, has damaged to different levels in the strained rebars depending on the amount of plastic pre-tensioning (Fig. 1c). Thus, it has been ensured that the actual surface condition at different locations in the tensile portion of a bend as shown in Fig. 1(a) is nearly simulated. The rebar has ferritic–pearlitic microstructure (Fig. 2a). Figure 2(b), (c), (d), (e) and (f) shows the typical high-resolution FE-SEM images of the steels (P1 to P5). It can be clearly seen in Fig. 2(b) that the cementite lamellae in a given pearlitic colony are oriented in a particular direction and are fairly straight (less bent). Since the orientations of different lamellae among pearlitic colonies could be different, their alignment with respect to the direction of tensioning is an important factor that affects the damage to the lamellae. However, as shown in Fig. 2(b), (c), (d), (e) and (f), as the extent of plastic pre-tensioning increases, the bending in the cementite lamellae also increases. If closely observed at some locations in P2 and P3 (Fig. 2c and d), local fracture of the lamellae can be seen (shown by dotted arrowheads). On the other hand, severely bent and fractured lamellae can be noticed in P4 and P5 (Fig. 2e and f) (shown by dotted circles). In fact, a significant kinking in the lamellae along with blunted fibers has also been observed in P5 (Fig. 2f). Thus, plastic pre-tensioning has resulted in a significant change in the microstructure of the rebar.

3.2 Electrochemical Behavior of the Rebar

3.2.1 Chloride-Free Pore Solutions (SCPS). The evolution of the OCP in SCPS is shown in Fig. 3(a). Stable potentials, as listed in Table 1, have been achieved in all the steels within the test duration. In the initial stages of electrochemical testing, non-negligible fluctuations have occurred in few specimens despite stabilizing their potentials for 1 week in SCPS. This could be due to the disturbances that might have occurred while connecting the specimen to the electrolytic cell (three-electrode arrangement) for further electrochemical testing. Interestingly, these fluctuations in P3 are considerably significant, which
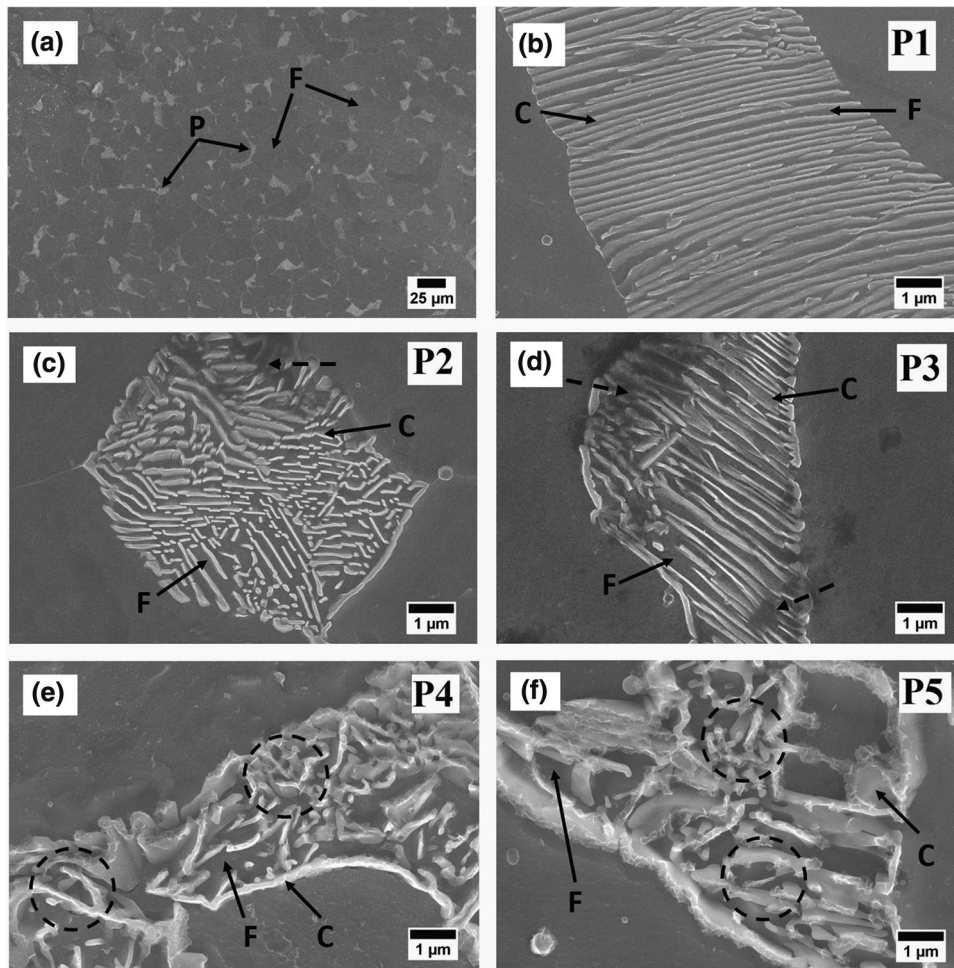
Fig. 2 FE-SEM micrographs of the unstrained rebar (P1) at (a) low magnification and (b) high magnification. (c–f) FE-SEM micrographs of various strained steels (P2-P5) (P, F and C shown with arrowheads represent the pearlite, ferrite and cementite, respectively)

could be attributed to their characteristic surface changes such as Lüders band formation and macrocell activity between exposed metal and damaged mill-scale, as explained in the subsequent sections. In the specimens in which the fluctuations of potentials have occurred (Fig. 3a), the OCP has increased initially, suggesting that the specimens are passivating due to high pH of SCPS. The cyclic polarization behavior of the steels in SCPS indicating activation-controlled mechanism is shown in Fig. 3(b), (c) and (d). The corrosion potentials (E_{corr}) of the unstrained and the strained specimens, denoting their thermo-dynamic stability in SCPS, are summarized in Table 1. To estimate the corrosion current densities (i_{corr}), Tafel extrapolation has been used, similar to the one reported by previous researches in a passivating environment like concrete pore solution (Ref 33, 35, 51), as (1) there were no signs of concentration polarization in the corroding system (Fig. 3b, c and d), and (2) the extrapolations of anodic and cathodic linear regions have coincided at the corrosion potential (E_{corr}), suggesting the limited possibility for the existence of multiple anodic Tafel slopes (cathodic loop). The corrosion current densities (i_{corr}) of the specimens along with their anodic and cathodic slopes estimated using Tafel extrapolation are also given in Table 1.

The Nyquist, Bode-magnitude and Bode-phase plots for the specimens are shown in Fig. 3e, f and g. Given the tendency to

form passive layer on the steel on which the mill-scale is present either completely or partially (depending on the level of strain (Fig. 1c)), a circuit having two time constants as shown in Fig. 3(e) was used in the analysis. The data pertaining to the plots have followed a very good fitting (χ^2 in the order of 10^{-3}) with respect to $R_s(Q_{dl}R_{ct})(Q_{ox}R_{ox})$, in which R_s is the solution resistance, Q_{dl} and R_{ct} are the constant phase element (CPE) and charge-transfer resistance of the double layer, and Q_{ox} and R_{ox} are the constant phase element (CPE) and resistance of the oxide layer on the steel. Taking the depressed semicircle behavior into consideration, the CPE has been used to model the capacitance instead of pure capacitor. The reactive term of the impedance is given by Eq. 3.

$$Z_{CPE} = Q^{-1}(j\omega)^{-n} \tag{Eq 3}$$

where Q is the admittance of the CPE, j is the imaginary unit representing the complex nature, n is the dispersion coefficient, and ω is the angular frequency.

Quantitative information of the electrochemical parameters extracted from the fitted EIS data is shown in Table 2. Both the CPE exponents (n_{ox} and n_{dl}) are obtained in the range of 0 to 1, suggesting the mixed behavior between ideal resistor and ideal capacitor (Table 2). In the absence of chlorides, the charge-transfer resistance of the specimens (R_{ct}) has been obtained in the range of 21,230 to 190,200 Ω cm^2 (Table 2). Simultaneously, the
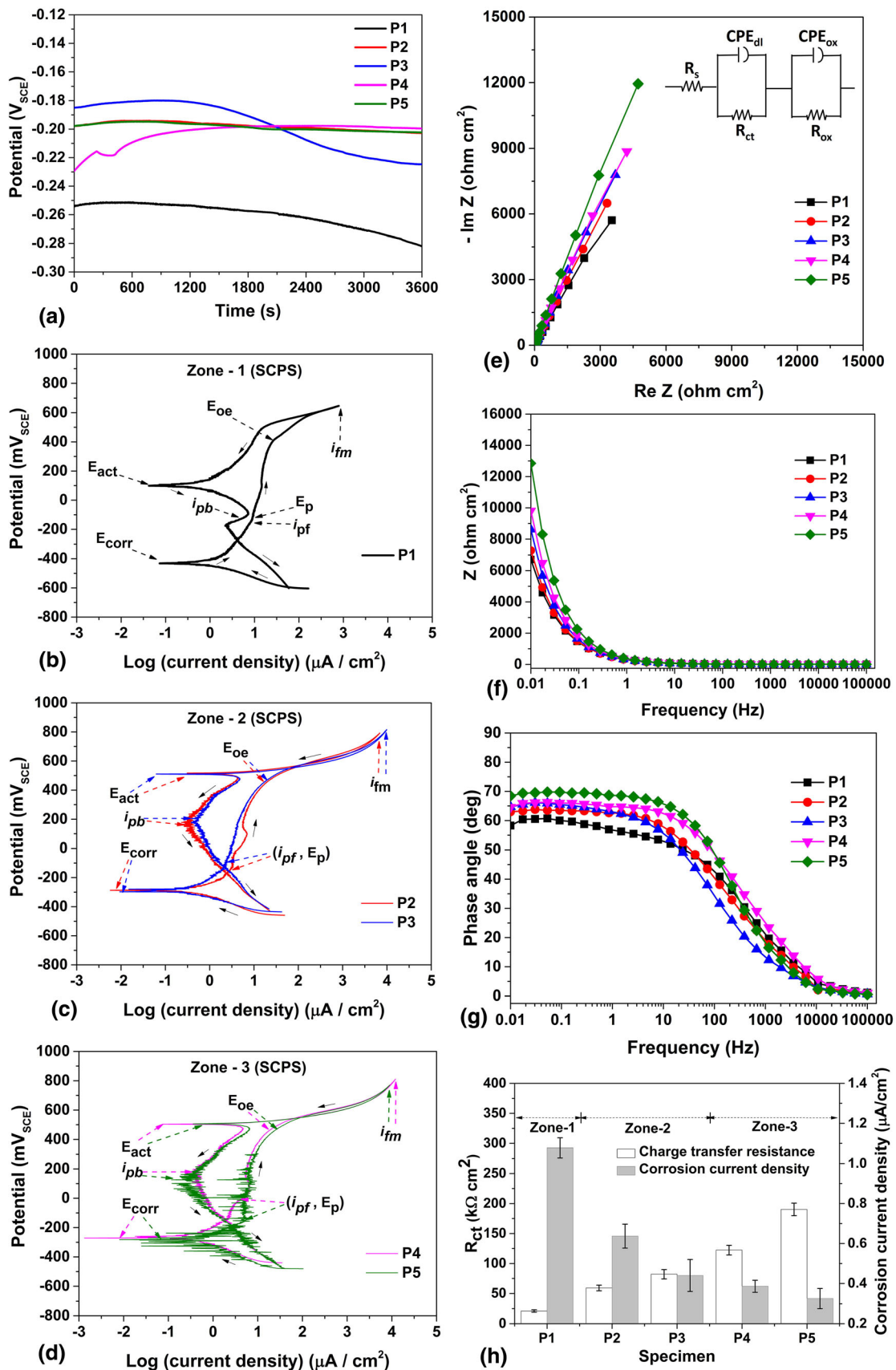
Fig. 3 (a) OCP (b–d) cyclic polarization behavior of the steels pertaining to zone-1 to zone-3 (e) Nyquist diagrams along with the EEC, (f) Bode-magnitude plots, (g) Bode-phase plots and (h) comparative corrosion behavior of strained steels in chloride-free pore solution (SCPS)

Table 1 Parameters measured for the steel specimens on the basis of cyclic polarization tests in the simulated concrete pore solution with and without chlorides

Specimen	OCP, mV_{SCE}	E_{corr}, mV_{SCE}	β_a, mV_{SCE}/decade	β_c, mV_{SCE}/decade	i_{corr}, $\mu A/cm^2$
SCPS					
P1	− 285 (14)	− 417 (30)	241 (77)	− 91 (10)	1.07 (0.05)
P2	− 211 (9)	− 275 (26)	164 (38)	− 117 (28)	0.64 (0.06)
P3	− 222 (11)	− 269 (19)	186 (30)	− 79 (18)	0.44 (0.08)
P4	− 201 (10)	− 277 (22)	207 (29)	− 86 (12)	0.38 (0.03)
P5	− 180 (9)	− 250 (24)	123 (24)	− 143 (21)	0.32 (0.05)
SCPS + Cl⁻					
P1	− 471 (10)	− 581 (17)	94 (29)	− 81 (28)	1.21 (0.09)
P2	− 478 (7)	− 597 (20)	112 (13)	− 96 (31)	1.26 (0.08)
P3	− 500 (12)	− 601 (18)	93 (20)	− 87 (12)	1.58 (0.12)
P4	− 527 (5)	− 583 (14)	88 (15)	− 223 (31)	2.10 (0.11)
P5	− 540 (9)	− 580 (12)	153 (13)	− 54 (71)	3.16 (0.10)

Deviations are mentioned in parentheses.

Table 2 Different electrochemical parameters obtained after fitting $R_s(Q_{ox}R_{ox})(Q_{dl}R_{ct})$ circuit to the EIS data of the steels in the simulated concrete pore solution with and without chlorides (error (%) is mentioned in parentheses)

Specimen	R_s, Ω cm^2	Q_{ox}, Ω^{-1} s^n cm^{-2}, $\times 10^{-4}$	n_{ox}	R_{ox}, Ω cm^2	Q_{dl}, Ω^{-1} s^n cm^{-2}, $\times 10^{-4}$	n_{dl}	R_{ct}, Ω cm^2
SCPS							
P1	7.19 (5.2)	5.30 (12.6)	0.79 (1.0)	93.15 (10.1)	10.18 (6.5)	0.80 (2.7)	21,230 (9.1)
P2	8.31 (3.8)	13.85 (9.8)	0.78 (0.5)	55.05 (4.3)	7.42 (4.7)	0.74 (3.0)	59,220 (8.3)
P3	8.95 (5.9)	23.14 (9.1)	0.79 (0.1)	51.23 (5.2)	9.56 (5.0)	0.73 (2.6)	82,070 (9.5)
P4	7.88 (2.6)	34.63 (10.8)	0.79 (0.6)	49.24 (8.1)	7.93 (3.6)	0.77 (3.8)	122,300 (6.7)
P5	7.12 (5.4)	35.39 (7.1)	0.80 (0.1)	45.62 (6.1)	6.80 (7.2)	0.79 (3.6)	190,200 (5.5)
SCPS + Cl⁻							
P1	3.92 (6.8)	28.62 (18.7)	0.80 (1.0)	20.86 (1.6)	22.42 (7.6)	0.65 (5.2)	5227 (4.1)
P2	3.67 (10.5)	23.13 (12.1)	0.79 (0.4)	19.73 (5.1)	24.15 (11.1)	0.68 (12.1)	4804 (3.8)
P3	3.80 (7.7)	35.63 (6.1)	0.78 (1.6)	21.38 (8.3)	27.55 (7.5)	0.69 (6.8)	4410 (3.1)
P4	2.94 (10.3)	36.68 (8.2)	0.83 (0.7)	14.32 (7.6)	29.86 (4.2)	0.75 (9.1)	3816 (5.6)
P5	3.43 (8.3)	39.57 (7.2)	0.80 (1.2)	7.21 (7.1)	36.05 (8.4)	0.80 (11.1)	2616 (4.7)

admittance of the double layer (Q_{dl}) in SCPS has decreased from 10.18×10^{-4} to 6.8×10^{-4} Ω^{-1} s^n cm^{-2} with the increase in pre-strain (Table 2). Shi et al. (Ref 12) have reported a charge-transfer resistance of 50,000 Ω cm^2 in SCPS for a mill-scale-coated low-carbon steel after 7 days of immersion in the solution, and thus, the R_{ct} values obtained in this study are in agreement with those reported in the literature (Ref 12).

It is worth mentioning that the presence of mill-scale, either in intact (unstrained) or damaged (strained) condition (Fig. 1c), would greatly inhibit the formation of passive layer on steels (Ref 12). From the values of R_{ox} in SCPS (Table 2), it can be inferred that the resistance offered by the strained steel toward the formation of passive layer has been greatly compromised due to the damage occurred to the mill-scale and has also reflected in the form of an increase in the admittance (Q_{ox}) of the oxide layer in the strained steels (Table 2). This would have eventually facilitated better passive layer formation on the strained steel as compared to the unstrained steel and have led to higher charge-transfer resistance in the former than the later.

The comparative corrosion behavior of the specimens in SCPS measured in terms of R_{ct} and i_{corr} is shown in Fig. 3(h), from which it can be inferred that in SCPS as the amount of pre-induced plastic strains increases, the charge-transfer resis-

tance (R_{ct}) of the rebar has also increased. As stated earlier, this behavior is related to the formation of the passive film in the steels. Generally, the increase in the magnitude of the impedance at low frequencies is due to the increase in the thickness of the passive film (Ref 52), provided all other test conditions are similar. In the present study, the specimens are different from each other only in the amount of pre-induced plastic strains and the corresponding changes occurred on their surface, and therefore, it can be understood that the pre-induced plastic strains in the rebar tend to form more protective and thickened passive films. Moreover, in SCPS, the stabilized OCP and the E_{corr} of the strained specimens have been obtained to be more positive than that of the unstrained specimen, thus indicating the higher thermodynamic stability of the passive films formed in the strained steels. Though a slight decrease in the corrosion current densities (i_{corr}) of all the strained steels as compared to the unstrained steels has been noticed, the behavior can be considered to be nearly comparable owing to the formation of fully developed passive films. This observation is in line with the literature in which lower current densities and more positive potentials of the steels under the action of sustained tensile stresses in SCPS have been reported due to the

Table 3 Electrochemical measurements of the steels on the basis of cyclic polarization in the simulated concrete pore solution with and without chlorides

Specimen	E_p, mV$_{SCE}$	E_{oe} or E_b, mV$_{SCE}$	i_{fm}, mA/cm^2	E_{act}, mV$_{SCE}$	i_{pf}, µA/cm^2	i_{pb}, µA/cm^2	DF
SCPS							
P1	− 100 (4)	440 (1)	1 (0.13)	105 (23)	9.89 (0.15)	3.16 (0.23)	0.32 (0.01)
P2	− 146 (8)	463 (5)	10 (0.04)	516 (6)	3.16 (0.25)	0.17 (0.10)	0.05 (0.02)
P3	− 147 (2)	465 (6)	10 (0.07)	516 (5)	1.77 (0.16)	0.31 (0.09)	0.18 (0.02)
P4	− 138 (4)	470 (2)	10 (0.10)	510 (2)	3.18 (0.26)	0.17 (0.08)	0.05 (0.02)
P5	− 165 (3)	477 (2)	10 (0.08)	510 (7)	3.98 (0.19)	0.10 (0.05)	0.02 (0.01)
SCPS + Cl⁻							
P1	− 380 (12)	− 366 (12)	1 (0.11)	− 568 (27)	15.2 (0.11)	1440 (215)	95 (13)
P2	− 440 (9)	− 322 (15)	1.78 (0.09)	− 726 (11)	16.4 (0.12)	3163 (320)	183 (17)
P3	− 452 (7)	− 137 (17)	1.99 (0.11)	− 709 (8)	17.1 (0.15)	5624 (352)	349 (18)
P4	− 451 (7)	61 (23)	2.51 (0.20)	− 719 (5)	18.2 (0.18)	7943 (450)	436 (20)
P5	− 442 (9)	227 (22)	10 (0.15)	− 645 (7)	22.3 (0.14)	12,589 (520)	564 (19)

Deviations are mentioned in parentheses.

increase in the semiconducting behavior of the passive films (Ref 11).

Other electrochemical parameters, such as passivation potential (E_p), oxygen evolution potential (E_{oe}), maximum anodic current density in the forward scan (i_{fm}), the potential of anodic-to-cathodic transition (E_{act}), the passive current densities in the forward scan (i_{pf}) and backward scan (i_{pb}), and damage factor (DF), are given in Table 3. While the E_p of the unstrained steel (P1) is more positive than that of the strained steels (P2-P5), the sudden increase in the current has occurred at almost the same potential at the test pH in all the steels ($E_{oe} \simeq 465$ mV), indicating the evolution of oxygen due to the decomposition of water. In all the strained steels, nearly the same range of passive region ($E_{oe} − E_P \simeq 612$ mV) has been observed before the evolution of oxygen. The range of passivity in the unstrained steel (P1) ($\simeq 540$ mV) is lower than that of the strained steels, and this also signifies the ability of forming denser and/or thicker passivated films in the later than the former.

After the potential corresponding to the evolution of the oxygen due to water splitting, the i_{fm} of the strained steels is about 10 times higher than that of the unstrained steel (Table 3). This gives rise to very interesting aspect of the electrochemical characteristic of iron oxide film at high anodic potentials. In general, there is a very high tendency for the oxide films to support oxygen evolution catalytically (Ref 53), and stronger the film, better would be the catalytic properties. For instance, Schäfer et al. (Ref 53) have reported excellent electrocatalytic behavior of supporting the oxygen evolution reaction by the oxidized surface of stainless steel at a pH of 13. Thus, the higher current densities (i_{fm}) after the oxygen evolution in the strained steels can be considered to be an indication of the formation of stronger passive films. Interestingly, Table 2 also shows increasing R_{ct} for the strained specimens, supporting greater double-layer resistance with gradual straining.

Furthermore, as shown in Fig. 3(b), (c) and (d), all the specimens have shown negative hysteresis in SCPS, i.e., the current densities in the reverse scan are less than that in the forward scan. In all the specimens, the potential of the anodic-to-cathodic transition (E_{act}) has been observed to be more positive than the corresponding corrosion potential (E_{corr}). This corroborates the fact that pits have not formed in pore solution. In addition, the E_{act} potentials of the strained steels are higher than that of the unstrained steel, though significant differences

among the individual strained steels have not been obtained. This indicates that the repassivating mechanism of the strained steels is thermodynamically more feasible. Furthermore, in all the specimens, the damage factor (DF) has been observed to be less than one, which implies that the passive film formed on the metal surface in SCPS is stable and protective. In other words, higher anodic polarization in SCPS has not resulted in a damage that promotes further degradation on the surface.

Moreover, the passive current densities of the strained steels in the forward scan (i_{pf}) and backward scan (i_{pb}) have been observed to be lower than that of the unstrained steel (P1) in SCPS (Table 3). Accordingly, the DF of a strained steel has been found to be lower than that of the unstrained steel in SCPS (Table 3), which indicates that in this electrolyte, the passivity developed on the surface of the strained steel is stronger than that of the unstrained steel. This, in turn, supports the understanding of more stable and thickened passive film formation in the strained steels as compared to the unstrained steel. The thickened passive film in the strained steel as compared to that in the unstrained steel has displaced the anodic Evans line in the former to lower current densities than that in the later (Fig. 3b, c and d). Therefore, lower DF values have been obtained in the strained steels as compared to the unstrained steel (Table 3).

It is well understood that the passive film is a hydrated iron oxidation film comprising Fe^{2+}, Fe^{3+} oxides and oxy-hydroxides (Ref 6). The formation and the stability of the passive film depend on the surface condition and the activity of the metal substrate underneath the film (Ref 6). It can be taken that the passive layer forming tendency is an indicative measure of the steel's initial corrosion susceptibility. The presence of mill-scale on the unstrained rebar (P1) offers a relatively better isolation to the metal surface from the bulk electrolyte, and therefore, relatively less influence of the underlying metal substrate by the anodic reaction could be expected. In the strained rebars, the surface condition is affected due to the damage to the mill-scale (Fig. 1c) and, thus, leads to the exposure of the bare metal, which increases their activity. In addition, the activity of the iron increases further due to the increase in the dislocation density (Ref 54, 55) and the change in the microstructure (Fig. 2b, c, d, e and f). Thus, the formation of more protective passive films in the strained steels can also be understood as an outcome of their high initial corrosion rates.

Furthermore, it has been reported by Karadakis et al. (Ref 56) that the composition of the pore solution that accumulates inside a fissure in the mill-scale is different from the bulk electrolyte due to local acidification and, thus, results in reduction of the pH in the neighborhood of the fissure. It has been well established that the lowered pH would result in high dissolution rate of the passive films, which eventually makes them thinner. This would have contributed to more negative potentials in the unstrained bar (P1). Based on the results obtained, the following mechanism for the formation of the passive film on the strained steel can be suggested. The formation rate of the film is higher than its corresponding dissolution rate at higher anodic potentials. In contrast, the difference between the above rates in an unstrained steel would have been relatively lower than that of the strained steel. This has led to the observations such as more noble OCP, spontaneous passivation and lower DF values in the strained steel as compared to the unstrained steel. In fact, the higher inhibiting effect of the protective passive film formed on the strained steel as compared to the unstrained steel toward polarization can be looked upon as a clear example of a corroding system where kinetics rules over thermodynamics. This can be understood from the very fact that despite the inherent tendency of the strained metal substrate to corrode (thermodynamic consideration), the protective passive film on its surface has inhibited the charge transfer (reaction kinetics) by acting as a diffusion barrier.

3.2.2 Chloride-Contaminated Pore Solutions (SCPS + Cl⁻).

The values of various electrochemical parameters of the steels in SCPS + Cl⁻ are summarized in Tables 1, 2 and 3, with the OCP of the specimens being shown in Fig. 4(a). Interestingly, the OCP has started going down with time. This typically reflects the weak surface film and rather continuous damage to the passive film and more active response. This is not the case for the OCP variation in SCPS without chloride ions (Fig. 3a), where spontaneous passivity is highly probable, and later, the spontaneous passivity has been observed in the cyclic polarization also (Fig. 3b, c and d). Moreover, it is important to mention that the level of chloride contamination in the concrete pore solution is very high (5% NaCl (by weight)), and therefore, the rebar would be under active corrosion process as soon as it comes in contact with this electrolyte. In such cases, immersing the specimen for longer duration in SCPS + Cl⁻ to acquire perfectly stable potential could result in unwanted corrosion on the surface of the rebar, and hence, the immersion time for stabilizing potentials was limited to 1 h only, despite the slight instability of potentials at the end of this period.

As expected, the addition of chlorides to the pore solutions has resulted in more negative potentials in all the steels as compared to their potentials in SCPS without chloride (Table 1). In general, as the amount of plastic strain increased, the OCP of the strained steels has become more negative, and the effect has been observed to be more pronounced at higher levels of pre-straining.

The cyclic polarization behavior of the steels in SCPS + Cl⁻ is shown in Fig. 4(b), (c) and (d). In general, the specimens have shown activation-controlled behavior. It can be seen in Fig. 4(b), (c) and (d) that the CP curves have shifted to higher current side as the amount of plastic strain increased. The corrosion potentials (E_{corr}) and the corrosion current densities (i_{corr}) of the specimens along with their anodic and cathodic slopes (estimated using Tafel extrapolation) are given in Table 1.

The Nyquist, Bode-magnitude and Bode-phase plots for the specimens in SCPS + Cl⁻ are shown in Fig. 4(e), (f) and (g). Similar to the analysis in SCPS, the EIS data in case of SCPS + Cl⁻ have also been fitted using $R_s(Q_{dl}R_{ct})(Q_{ox}R_{ox})$ (Fig. 4f), and the information extracted from the fitted data is summarized in Table 2. The addition of chlorides to the pore solution has not only resulted in the decrease in R_{ox} values, but also led to the increase in the admittance of the oxide layer Q_{ox} (Table 2). The values of charge-transfer resistance of the specimens (R_{ct}) in SCPS + Cl⁻ have been obtained in the range of 2616 to 5227 Ω cm^2 (Table 2), and thus, it can be stated that the addition of chlorides has resulted in an enormous reduction in the R_{ct} of the steels in SCPS + Cl⁻ as compared to that in SCPS (Table 2). This reduction in the resistance has been accompanied with the simultaneous increase in the admittance of the double layer (Q_{dl}) (Table 2).

The comparative corrosion behavior of the specimens in SCPS + Cl⁻, measured in terms of R_{ct} and i_{corr}, is shown in Fig. 4(h), from which it can be inferred that as the amount of pre-induced plastic strains increased, the corrosion susceptibility of the rebar has also increased. This can be understood as the result of localized breakdown of the fully developed passive films in SCPS by the chlorides, which have exposed the underlying steel for further dissolution. In this regard, it is worth iterating that the specimens were first exposed to SCPS for 7 days in order to form stable passive film. The susceptibility of the locally depassivated steel to corrosion, being a kinetic property, depends on the condition of the electrode surface and the extent of galvanic couples formed between the fragmented cementite and ferrite microstructurally. In case of the strained steels, due to fragmentation of cementite (Fig. 2c, d, e and f), the effective cathodic activity has increased, which has demanded higher metal dissolution from the neighboring ferrite. Moreover, chloride ions act as damaging species to passive film. Furthermore, the bare metal is directly exposed to aggressive chlorides in the strained specimens, i.e., the specimens are either partially or completely devoid of mill-scale as observed in Fig. 1(c). This has resulted in obtaining higher corrosion rates in the strained steels. It can be understood that though the same surface condition prevails in the strained steel specimens in SCPS without Cl⁻ ions, the passivity is highly compromised in the presence of Cl⁻ ion, as explained in the subsequent discussion.

Another important factor, which needs special mention, is the presence of passive layer on these steels in the non-affected portion. The addition of chlorides would create a locally dissimilar environment on the surface, which could lead to the increased tendency of galvanic cell formation between passivated part and the chloride-attacked part locally. Since the passive films formed in the strained steels before the addition of chlorides are more protective, such galvanic couple formation would be stronger in the strained steels. This is reflected in the form of greater corrosion tendency in them in the presence of chlorides. It is important to mention that the steel specimens have been exposed to SCPS for 7 days for the stabilization of surface film. Hence, it is very clear that Cl⁻ ions are active negatively on the stability of the passive film.

Principally, more negative E_{corr} values have been obtained in the strained specimens, though some slight ennoblement has occurred at higher levels of pre-straining (Table 1). This ennoblement could be understood by considering the synergis-
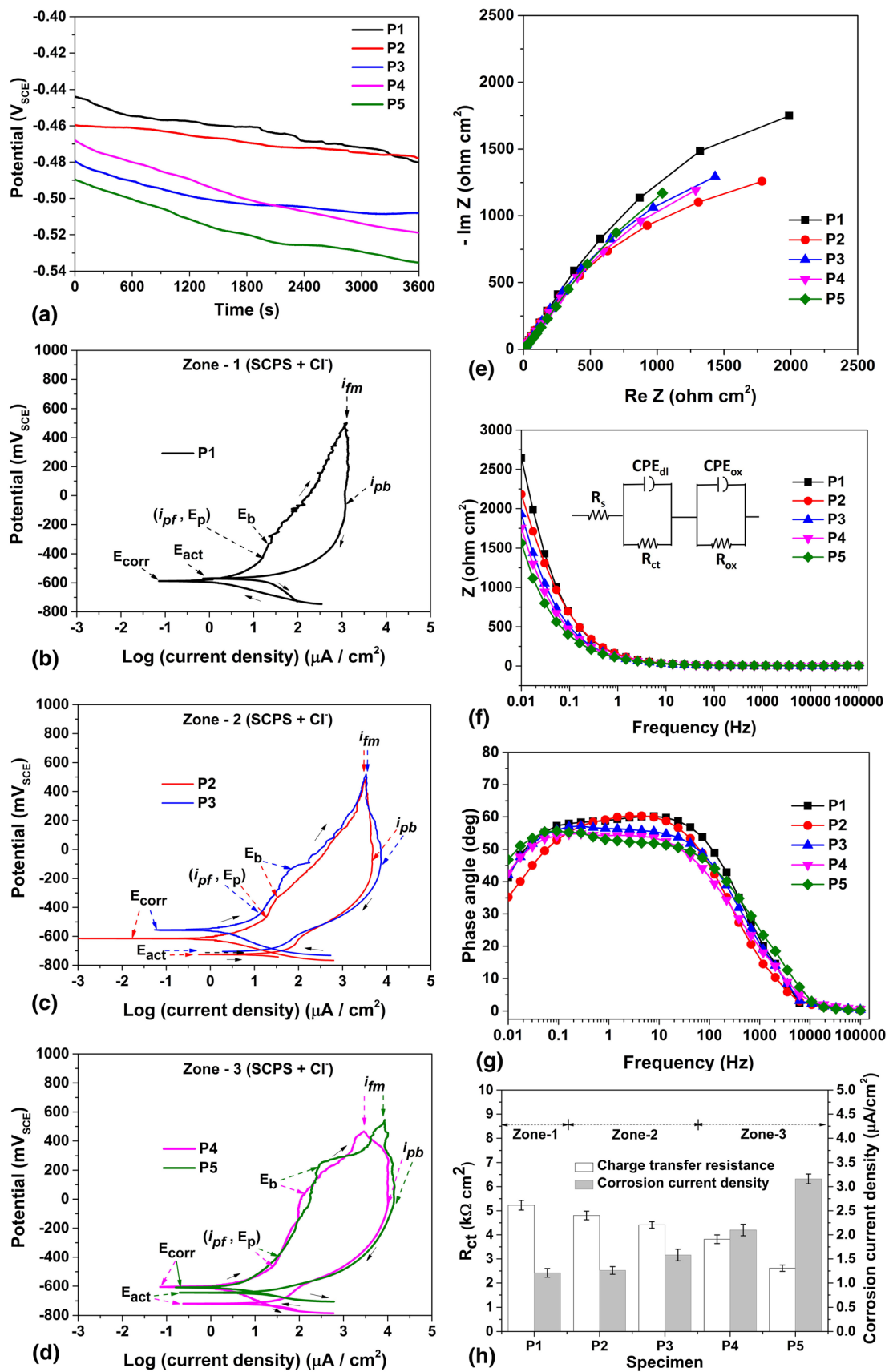
Fig. 4 (a) OCP, (b–d) cyclic polarization behavior of the steels pertaining to zone-1 to zone-3, (e) Nyquist diagrams, (f) Bode-magnitude plots along with the EEC, (g) Bode-phase plots and (h) comparative corrosion behavior of strained steels in chloride-contaminated pore solution (SCPS + Cl⁻)

tic effect of two important factors on the stability of the specimens from thermodynamics viewpoint, i.e., the dislocation density and the galvanic action due to partially damaged mill-scale in some of the strained specimens. Pre-tensioning the rebar in the easy-slip zone, i.e., zone-2, would result in the generation of dislocations, which tend to appear on the surface as Lüders band (Ref 55). Simultaneously, relaxation of the already existing point defects in the Cottrell atmosphere would also take place in this zone due to pre-tensioning. But at higher levels of pre-straining, the relaxation becomes insignificant as compared to the increase in dislocations. Particularly, in P3, full formation of the bands takes place due to increased dislocation density. This, in turn, results in a significant surface variation as compared to the unstrained specimen, as shown in the high-resolution FE-SEM micrographs of un-etched specimens (Fig. 5a and b).

Since the specimens were un-etched, distinctive features, such as grain boundaries and cementite lamellae, are not clearly visible in these micrographs (Fig. 5a and b). However, it can be seen that a few cluster-like structures are present at some locations (Fig. 5a and b). This could be the pearlite colonies dispersed in the ferrite matrix. Furthermore, the formation of the Lüders band in the strained specimen (P3) has been confirmed through the distinctive appearance of black stretch marks on its surface (Fig. 5b). A close observation of Fig. 5(b) also gives an insight that the angle of the stretch mark is around 45° from the horizontal, which is the maximum shear plane arising on account of uniaxial tensioning. Moreover, in these specimens (P2 and P3), the galvanic activity between the scaled and un-scaled portions is also significant, which has resulted in greater thermodynamic instability. Hence, relatively more negative corrosion potentials have been obtained in them (Table 1). In case of the specimens P4 and P5 (zone-3), though the dislocation density near the grain boundaries increases, the tendency to form the galvanic cell between scaled and un-scaled portion reduces, as the specimens are characterized with complete removal of mill-scale (Fig. 1c). Therefore, relatively positive potentials have been obtained in the specimens pertaining to zone-3 (Table 1). However, the E_{corr} of P5 is lower than that of P1, as the potentials of the former represent the behavior of the strained steel without any mill-scale (Table 1).

The breakdown potential (E_b) of P1 is close to its passivation potential (E_p), which indicates that its passivity is very limited (Fig. 4b). Figure 5(c) shows the specimen P1 at the end of the CP test. If it is closely observed, it can be noticed that the entire surface has not corroded, which has reflected in the form of limited passivity behavior. Furthermore, at several locations in P1, the mill-scale is also intact at the end of the test (Fig. 5c). This shows that these steel specimens corresponding to P1 are not susceptible to corrosion easily. On the other hand, the passivation potentials (E_p) of the strained steels (P2-P5) are relatively more negative than that of the unstrained steel (P1) (Table 3). Though considerable differences in the E_p among the strained steels have not been observed, the breakdown (E_b) has occurred at different potentials in them (Table 3). Fair range of passivity has been exhibited by all the strained steels except P2, whose range is very close to P1. This could be attributed to the presence of mill-scale on the surface of P2, which has not damaged considerably when compared to other strained specimens (Fig. 1c). Thus, the surface condition of P1 and P2 is nearly the same, which has resulted in obtaining almost equal passivity in them (Fig. 5e). The surface of a typical strained

specimen (P5) has been observed to be fully covered with corrosion products (Fig. 5d), thus confirming their passivity behavior. Moreover, from Fig. 4(b), (c) and (d), it can be observed that in the passive region, the corrosion density is not strictly constant. This indicates that the corrosion products formed on the surface have not completely isolated the steel from the electrolyte, which can be attributed to the Cl^- ion.

Interestingly, as shown in Fig. 5(e), higher range of passivity (measured as $E_b - E_p$) has been obtained in the specimens having higher amount of plastic strain. This could be because of their high initial corrosion rates, which has led to the complete covering of the surface with corrosion products, thereby minimizing the possibility of further attack on the metal specimen. Indeed, exhibiting higher passivity by the strained specimen also signifies its tendency to form protective passive film similar to the observation made in SCPS.

In general, as shown in Fig. 4(b), (c) and (d), the specimens have shown positive hysteresis in SCPS + Cl^-, i.e., the current densities in the reverse scan are more than that in the forward scan. This denotes that the passive film has been damaged due to the formation of pits in the presence of chlorides. While the anodic-to-cathodic transition potential (E_{act}) of the unstrained steel (P1) has almost coincided with its corrosion potential (E_{corr}), the E_{act} of the strained steels is less noble than their corresponding E_{corr} values. This indicates that the pits have not recuperated, and there exists an inherent tendency for the corroded-strained surface to support the formation of new pits. The thermodynamic instability of the corroded surface, evaluated as the difference between E_{act} and E_{corr} (pit instability), is higher in the strained steels as compared to the unstrained steel (Fig. 5f). A close observation of Fig. 4(b), (c) and (d) also reveals that the current densities corresponding to E_{act} are higher than i_{corr}.

After the breakdown, the bare metal would be directly exposed to chlorides, and therefore, the inherent corroding tendency of the steel can be comprehended from the current densities obtained after E_b. The maximum anodic current density in the forward scan (i_{fm}) of the strained steel is higher than that of the unstrained steel (Fig. 4(b), (c) and (d) and Table 3) and nearly proportional to the amount of plastic strain. This observation reinforces the understanding that the corrosion susceptibility of the steels increases with the amount of plastic strain in chloride-contaminated pore solution.

Moreover, in the strained steels, the anodic current densities in the reverse scan are higher than their corresponding i_{fm} values (Fig. 4b, c and d). The extent of shift in the current during the reverse scan has also increased with the amount of plastic strain. Furthermore, the passive current densities of the strained steels in the forward scan (i_{pf}) and backward scan (i_{pb}) have been observed to be higher than that of the unstrained steel (P1) (Table 3). In all the steels, the DF is more than one, which denotes that their surfaces have significantly damaged and have shown limited repassivating effect due to presence of Cl^- ions. Particularly, the DF of the strained steels is higher than that of an unstrained steel (Fig. 5(f) and Table 3). This denotes the higher tendency of the corroded surface of the strained steel to support further degradation as compared to that of an unstrained steel. Thus, not only the corrosion current density (i_{corr}), other electrochemical parameters, such as maximum anodic current density in the forward scan (i_{fm}), DF and pit-instability factor also confirm the higher corroding tendency of the strained steel in chloride-contaminated pore solution as compared to the unstrained steel.
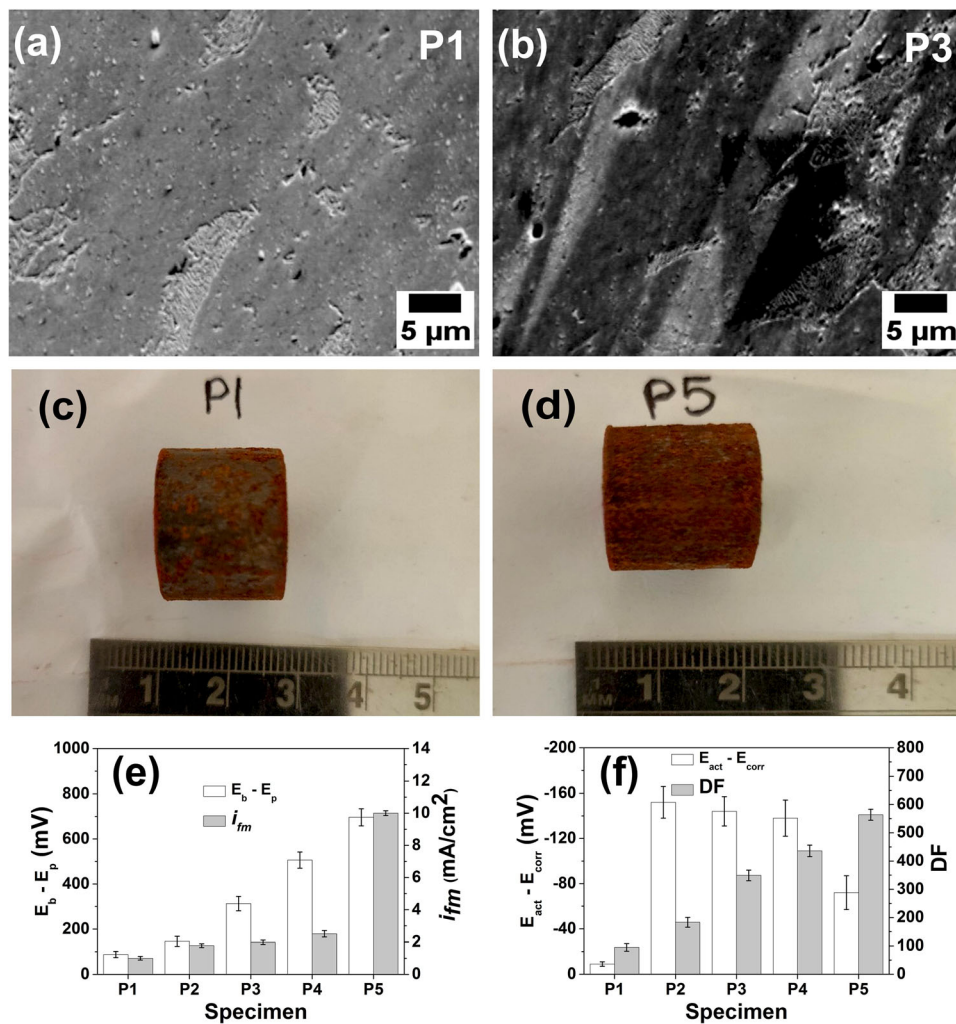
Fig. 5 High-resolution FE-SEM images obtained without etching the surface of the polished (a) P1 and (b) P3 steels. (c) P1 and (d) P5 specimens at the end of CP tests in chloride-contaminated pore solution. (e and f) Corrosion behavior of the steels characterized in terms of (e) range of passivity ($E_b - E_p$) and maximum current density in the anodic branch during forward scan (i_{fm}), (f) thermodynamic stability ($E_{act} - E_{corr}$) and the damage factor (DF) of the surface at the end of CP tests in chloride-contaminated pore solution

Typical optical micrographs of the curved surface of some specimens at the end of CP tests in chloride-contaminated pore solution are shown in Fig. 6(a), (b), (c) and (d). From the micrographs, it is clearly evident that the attack in the strained specimen (P5) (Fig. 6c and d) is higher than that of the unstrained specimen (Fig. 6a and b). While the chloride attack in the unstrained specimen is very localized (Fig. 6a and b), the attack in case of the strained specimen appears to be uniform (Fig. 6c and d). This is an indicative measure of the higher pitting density in the later as compared to the former. In brief, the pitting tendency of the strained steel is higher than that of the unstrained steel.

Figure 7(a) and (b) shows the FTIR and Raman spectroscopy of the rust collected from the specimens at the end of cyclic polarization tests in chloride-contaminated pore solution. The dip at the wave number 466 cm^{-1} in FTIR spectra (Ref 49) and the peak at a Raman shift (Ref 49) of 220 cm^{-1} correspond to hematite (α-Fe$_2$O$_3$), whereas the dip at 1020 cm^{-1} in FTIR spectra and the peaks at 280 and 1311 cm^{-1} denote the presence of lepidocrocite (γ-FeOOH) (Ref 49). Similarly, the presence of akaganeite (β-FeOOH) and goethite (α-FeOOH) has been confirmed from the broader dips at 630-700 cm^{-1} and

800-900 cm^{-1} in the FTIR spectra, respectively (Ref 49). Furthermore, the presence of goethite (α-FeOOH) has been indicated by the peaks at 380 and 560 cm^{-1} in the Raman spectra (Ref 49), while that of akaganeite (β-FeOOH) has been observed at a Raman shift of 388 and 720 cm^{-1}. It can easily be comprehended that the observed wave numbers of the phases are very close to the characteristic ones reported in the literature (Ref 49) with very little or no deviation. The proportion of different phases in various rust samples obtained by the deconvolution of the FTIR spectra is given in Table 4.

Closer examination of the individual proportions (Fig. 7(a) and Table 4) reveals that there exists a substantial proportion of akaganeite (β-FeOOH) on the surface of the corroded specimen due to the presence of significant chlorides in the test solution. It is worth mentioning that the formation of akaganeite (β-FeOOH) requires direct interaction of chloride ions with Fe in the presence of oxygen and moisture (Ref 42). The amount of akaganeite (β-FeOOH) has increased in the strained steel indicating the vulnerability of its metal substrate to chloride-induced corrosion after the breakdown of the passive film. Since the strained steels are highly active than the unstrained steel, chlorides can easily be adsorbed on their surface.
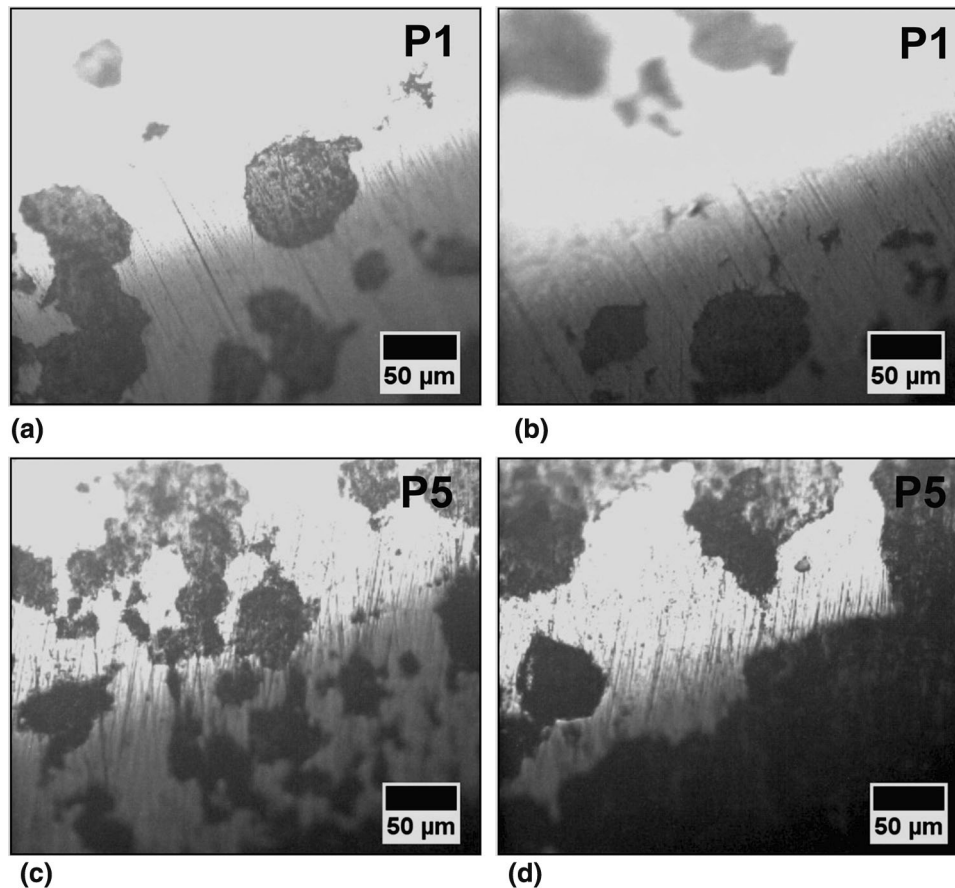
Fig. 6 Optical micrographs of the corroded surfaces of the (a and b) unstrained (P1) and (c and d) strained specimens (P5) at the end of CP tests in chloride-contaminated pore solution. Higher attack in the strained specimen (P5) as compared to an unstrained specimen (P1) can be seen. The rounded nature of the surface does not allow complete focus all around the region

Therefore, higher amount of akaganeite (β-FeOOH) has been obtained in the strained steels (Table 4). On the other hand, the proportion of goethite (α-FeOOH), a stable oxy-hydroxide phase, has been observed to decrease at higher levels of plastic strain. Since the experiments have been carried out in a freely aerated system, the proportion of lepidocrocite (γ-FeOOH) has been found to be significant, though no specific relation between their proportions and the amount of plastic strains has been obtained.

The α/γ* value of the rust evaluated using Eq. 4 is listed in Table 4. The higher the α/γ* value, the higher would be its protective nature (Ref 50).

$$\frac{\alpha}{\gamma^*} = \frac{Area\,of\,the\,dip\,in\,between\,800-900cm^{-1}}{Sum\,of\,areas\,of\,the\,dips\,obtained\,at\,1020cm^{-1}\,and\,630-700cm^{-1}}$$
(Eq 4)

The variation of the protective ability (α/γ* value) of the rusts remained on the surface of different specimens after performing CP tests is shown in Fig. 7(c). In general, the corrosion products that have finally remained on the strained steels at the end of the CP tests in SCPS + Cl⁻ have been observed to be less protective in nature (lower α/γ* value) as compared to the phases remained on the unstrained steels. Higher levels of pre-straining have resulted in the formation of more un-protective rust (Table 4). This can be attributed to the predominant presence of akaganeite (β-FeOOH) in the rust

samples pertaining to strained steels. In other words, if the passivity is compromised due to chlorides, the rust on the strained steel would become un-protective as compared to that of the unstrained steel since chlorides can be easily adsorbed on strained steels due to their highly active surface. The un-protective rust on the strained steel would have also contributed in obtaining high current densities after the breakdown of the passivity in them.

A comprehensive understanding on the mechanism involved in the corrosion of the unstrained and strained rebars in concrete environment, which are later subjected to chloride attack gradually, is schematically shown in Fig. 8(a), (b), (c), (d), (e), (f), (g), (h), (i) and (j). An unstrained rebar (Fig. 8a) is characterized with the presence of mill-scale on the surface and the usual arrangement of cementite lamellae in pearlite colony. A strained bar (Fig. 8b) differs from the unstrained bar in three ways: (1) surface exposure to the electrolyte due to partial or complete removal of mill-scale, (2) arrangement of cementite lamellae and (3) dislocation density. When exposed to a highly passivating environment, like pore solution, mimicking the electrolytic condition of concrete before the chloride attack, stronger passive films would be formed in the strained steel as compared to the unstrained steel (Fig. 8c and d). This is primarily due to the inherent tendency of the strained steel to corrode faster. Based on the charge-transfer resistance, maximum anodic current density after the oxygen evolution and the DF of the steels obtained in SCPS in this study, it could also be
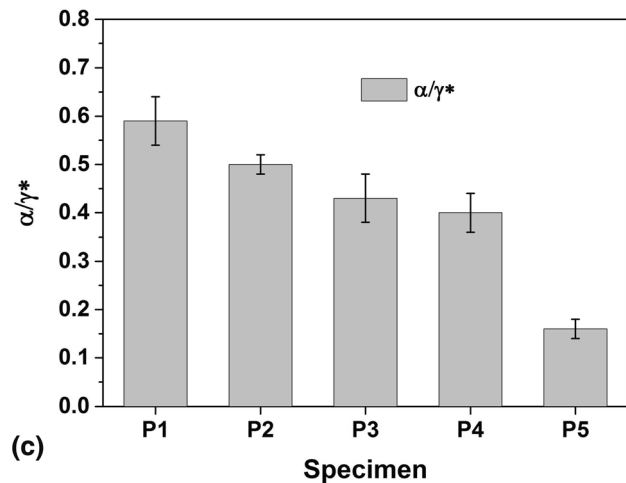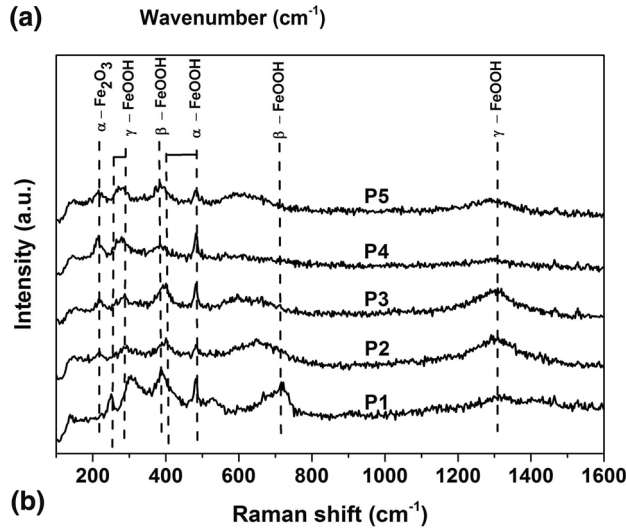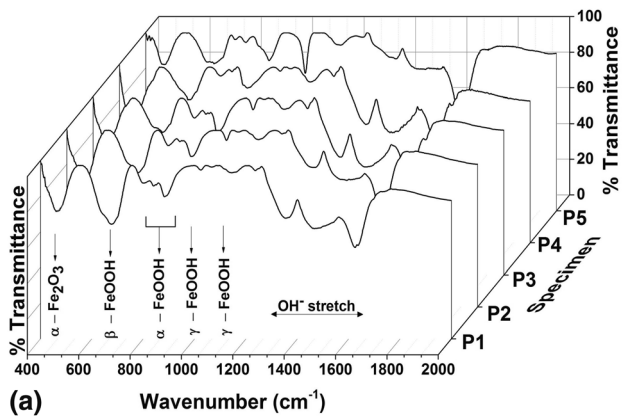
Fig. 7 (a) FTIR spectra, (b) Raman spectra and (c) α/γ* ratio of the rust collected from the specimens after performing the CP tests in chloride-contaminated pore solution

Table 4 Quantifying the rust products observed in the FTIR spectra and the α/γ* ratio indicating the protective ability in chloride-contaminated pore solution

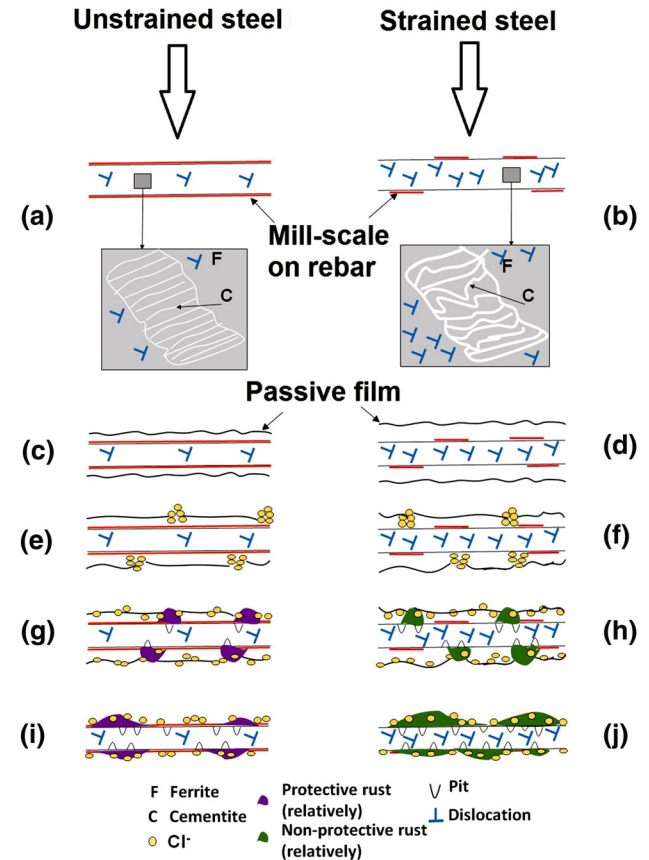| Specimen	Rust phases and their relative proportion				
	α-Fe_2O_3	β-FeOOH	α-FeOOH	γ-FeOOH	α/γ*
P1	1123	1146	882	312	0.59 ± 0.05
P2	1026	1337	855	375	0.50 ± 0.02
P3	1203	1467	826	309	0.46 ± 0.05
P4	1352	1870	796	120	0.40 ± 0.04
P5	1253	3099	553	415	0.16 ± 0.02

Fig. 8 Schematic representation of the mechanisms involved in the corrosion of the unstrained and the strained steels subjected to chloride attack in the concrete environment

hypothesized that the thickness of the passive film formed in the strained steel would be slightly higher than that of the unstrained steel. In SCPS, both the unstrained and strained steels have low pitting susceptibility.

However, in the presence of chlorides (Fig. 8e and f), the tendency to form galvanic cells would be higher in the strained steel as compared to that of the unstrained steel due to several factors that are electrochemically dissimilar in the former case, such as the scaled and unscaled portions, densely passivated and depassivated surface, and fragmented cementite and ferrite.

In addition, the increase in dislocation density also contributes to higher corrosion susceptibility of the strained steel as compared to that of the unstrained steel in chloride containing SCPS. At any given stage, due to the above-mentioned factors, the amount of corrosion in the strained steel would be higher than that in the unstrained steel. This would lead to a condition in which thicker but discontinuous rust forms on the strained steel as compared to that of unstrained steel (Fig. 8g, h, i and j). This has reflected in the form of higher range of passivity in the strained steel as compared to the unstrained steel (Fig. 4d, e and f).

Nevertheless, if the passivated surface is damaged by chlorides (i.e., after breakdown) the corrosion current would be higher in case of the strained steel than the unstrained steel. Though in both the cases, the pits would continue to grow, the tendency for pit formation would be very high in the strained steel than in the unstrained steel. The corrosion products formed on the surface of the strained steel would be unprotective due to the higher amount of akaganeite (β-FeOOH) in the rust (Fig. 8g, h, i and j) and, thus, support higher current density and pitting in them.

Similar phenomenon of increased passivating ability of steel specimens in SCPS under sustained tensile stress has been reported by Zhang and Poursaee (Ref 11). However, when the pore solutions are contaminated with chlorides (i.e., SCPS + Cl⁻), higher corrosion tendency in the stressed specimens has been observed by them. The results of the present study, which exclusively describe the corrosion behavior of rebars having pre-induced plastic strains, are in accordance with the results reported on the corrosion behavior under sustained tensile loads. However, the present analysis categorically explains the effect of pre-induced plastic strain, since other factors, such as the composition of the rebar, its initial microstructure and composition of the electrolyte, are constant in all the tests. Moreover, the variation in corrosion mechanism at different stages of strained conditions has also been comprehensively and uniquely discussed.

4. Conclusions

The work clearly brings out the relative corrosion behavior of the rebar in the strained and unstrained condition in simulated concrete pore solution with and without chloride contamination. Electrochemical measurements in chloride-free pore solution (SCPS) have shown that the passive film formed on a strained steel would be more protective in nature as compared to that in unstrained steel due to faster kinetic film formation on the surface of the strained bar. This has been indicated by the increase in the charge-transfer resistance and the simultaneous reduction in the corrosion current density of the rebar in SCPS upon inducing plastic strains.

On the other hand, in chloride-contaminated pore solution (SCPS + Cl⁻), with the increase in the amount of plastic strains, the corrosion susceptibility of the steel has increased. This is due to the localized depassivation of the surface by chlorides. In addition, the strained steels have shown higher maximum current densities (i_{fm}) and less noble E_{act} as compared to that of the unstrained steels in SCPS + Cl⁻, which denote the higher pit instability in them. The increased corrosion susceptibility of the strained steel substrate is also a strong function of the change in the surface condition, the microstructure of the rebar and the weak characteristic of the oxide film with lesser protective index indicated by its lower α/γ^* value as compared to the unstrained one.

References

1. Z.P. Bazant, Physical Model for Steel Corrosion in Concrete Sea Structures: Theory, *J. Struct. Div.*, 1979, **105**(ST6), p 1137–1153

2. A. Poursaee, Corrosion of Steel Bars in Saturated Ca(OH)₂ and Concrete Pore Solution, *Concr. Res. Lett.*, 2010, **1**(3), p 90–97

3. S. Mundra, M. Criado, S.A. Bernal, and J.L. Provis, Chloride-Induced Corrosion of Steel Rebars in Simulated Pore Solutions of Alkali-Activated Concretes, *Cem. Concr. Res.*, 2017, **100**, p 385–397

4. M. Saremi and E. Mahallati, A Study on Chloride-Induced Depassivation of Mild Steel in Simulated Concrete Pore Solution, *Cem. Concr. Res.*, 2002, **32**, p 1915–1921

5. P. Ghods, O.B. Isgor, G.A. McRae, and G.P. Gu, Electrochemical Investigation of Chloride-Induced Depassivation of Black Steel Rebar Under Simulated Service Conditions, *Corros. Sci.*, 2010, **52**, p 1649–1659

6. P. Ghods, O. Burkan Isgor, F. Bensebaa, and D. Kingston, Angle-Resolved XPS Study of Carbon Steel Passivity and Chloride-Induced Depassivation in Simulated Concrete Pore Solution, *Corros. Sci.*, 2012, **58**, p 159–167

7. L. Li and A.A. Sagüés, Chloride Corrosion Threshold of Reinforcing Steel in Alkaline Solutions-Cyclic Polarization Behaviour, *Corrosion*, 2002, **58**(4), p 305–316

8. L.T. Mammoliti, L.C. Brown, C.M. Hansson, and B.B. Hope, The Influence of Surface Finish of Reinforcing Steel and pH of the Test Solution on the Chloride Threshold Concentration for Corrosion Initiation in Synthetic Pore Solutions, *Cem. Concr. Res.*, 1996, **26**, p 551–556

9. R.R. Hussain, J.K. Singh, A. Alhozaimy, A. Al-Negheimish, C. Bhattacharya, R.S. Pathania, and D.D.N. Singh, Effect of Reinforcing Bar Microstructure on Passive Film Exposed to Simulated Concrete Pore Solution, *ACI, Mater. J.*, 2018, **115**(2), p 181–190

10. J. Williamson and O.B. Isgor, The Effect of Simulated Concrete Pore Solution Composition and Chlorides on the Electronic Properties of Passive Films on Carbon Steel Rebar, *Corros. Sci.*, 2016, **106**, p 82–95

11. Y. Zhang and A. Poursaee, Passivation and Corrosion Behavior of Carbon Steel in Simulated Concrete Pore Solution under Tensile and Compressive Stresses, *J. Mater. Civ. Eng.*, 2015, **27**(8), p 1–9

12. J. Jie Shi and J. Ming, Influence of Mill Scale and Rust Layer on the Corrosion Resistance of Low-Alloy Steel in Simulated Concrete Pore Solution, *Int. J. Miner. Metall. Mater.*, 2017, **24**(1), p 64–74

13. T. Yonezawa, V. Ashworth, and R.P.M. Procter, Pore Solution Composition and Chloride Effects on the Corrosion of Steel in Concrete, *Corrosion*, 1988, **44**(7), p 489–499

14. M. Moreno, W. Morris, M.G. Alvarez, and G.S. Duffó, Corrosion of Reinforcing Steel in Simulated Concrete Pore Solutions Effect of Carbonation and Chloride Content, *Corros. Sci.*, 2004, **46**, p 2681–2699

15. R.B. Figueira, A. Sadovski, A.P. Melo, and E.V. Pereira, Chloride Threshold Value to Initiate Reinforcement Corrosion in Simulated Concrete Pore Solutions: The Influence of Surface Finishing and pH, *Constr. Build. Mater.*, 2017, **141**, p 183–200

16. K. Tuuti, *Corrosion of Steel in Concrete*, Swedish Cement and Concrete Research Concrete Research Institute, Stockholm, 1982

17. M. Raupach, Investigations on the Influence of Oxygen on Corrosion of Steel in Concrete—Part l, *Mater. Struct. Constr.*, 1996, **29**, p 174–184

18. R.G. Pillai and D. Trejo, Surface Condition Effects on Critical Chloride Threshold of Steel Reinforcement, *ACI, Mater. J.*, 2005, **102**(2), p 103–109

19. U. Angst, B. Elsener, C.K. Larsen, and Ø. Vennesland, Critical Chloride Content in Reinforced Concrete—A review, *Cem. Concr. Res.*, 2009, **39**, p 1122–1138

20. Y. Liu and R.E. Weyers, Modeling the Time-to-Corrosion Cracking in Chloride Contaminated Reinforced Concrete Structures, *ACI, Mater. J.*, 1998, **95**(6), p 675–681

21. D. Chen and S. Mahadevan, Chloride-Induced Reinforcement Corrosion and Concrete Cracking Simulation, *Cem. Concr. Compos.*, 2008, **30**, p 227–238

22. B.H. Oh, K.H. Kim, and B.S. Jang, Critical Corrosion Amount to Cause Cracking of Reinforced Concrete Structures, *ACI, Mater. J.*, 2009, **106**(4), p 333–339

23. L. Chernin, D.V. Val, and K.Y. Volokh, Analytical Modelling of Concrete Cover Cracking Caused by Corrosion of Reinforcement, *Mater. Struct. Constr.*, 2010, **43**(4), p 543–556

24. S. Yoon, K. Wang, W.J. Weiss, and S.P. Shah, Interaction Between Loading, Corrosion, and Serviceability of Reinforced Concrete, *ACI, Struct. J.*, 2000, **97**(6), p 637–644

25. T. El Maaddawy, K. Soudki, and T. Topper, Long-Term Performance of Corrosion-Damaged Reinforced Concrete Beams, *ACI, Struct. J.*, 2005, **102**(5), p 649–656

26. G. Malumbela, M. Alexander, and P. Moyo, Steel Corrosion on RC Structures Under Sustained Service Loads—A Critical Review, *Eng. Struct.*, 2009, **31**, p 2518–2525

27. A. Ababneh and M. Sheban, Impact of Mechanical Loading on the Corrosion of Steel Reinforcement in Concrete Structures, *Mater. Struct. Constr.*, 2011, **44**, p 1123–1137

28. Y. Du, M. Cullen, and C. Li, Structural Effects of Simultaneous Loading and Reinforcement Corrosion on Performance of Concrete Beams, *Constr. Build. Mater.*, 2013, **39**, p 148–152

29. J. Dong, Y. Zhao, K. Wang, and W. Jin, Crack Propagation and Flexural Behaviour of RC Beams Under Simultaneous Sustained Loading and Steel Corrosion, *Constr. Build. Mater.*, 2017, **151**, p 208–219

30. C. Fu, N. Jin, H. Ye, X. Jin, and W. Dai, Corrosion Characteristics of a 4-year Naturally Corroded Reinforced Concrete Beam with Load-Induced Transverse Cracks, *Corros. Sci.*, 2017, **117**, p 11–23

31. R.R. Aveldaño and N.F. Ortega, Behavior of Concrete Elements Subjected to Corrosion in Their Compressed or Tensed Reinforcement, *Constr. Build. Mater.*, 2013, **38**, p 822–828

32. X. Feng, Y. Tang, and Y. Zuo, Influence of Stress on Passive Behaviour of Steel Bars in Concrete Pore Solution, *Corros. Sci.*, 2011, **53**, p 1304–1311

33. X. Feng, X. Lu, Y. Zuo, N. Zhuang, and D. Chen, Electrochemical Study the Corrosion Behaviour of Carbon Steel in Mortars Under Compressive and Tensile Stresses, *Corros. Sci.*, 2016, **103**, p 66–74

34. H. Li and X. Wu, Effect of Tension Strain Level on Reinforcement Corrosion, *J. Mater. Civ. Eng.*, 2018, **30**(3), p 1–8

35. J. Shi, J. Ming, W. Sun, and Y. Zhang, Corrosion Performance of Reinforcing Steel Under Simultaneous Flexural Load and Chlorides Attack, *Constr. Build. Mater.*, 2017, **149**, p 315–326

36. F. Li, Y. Yuan, and C.Q. Li, Corrosion Propagation of Prestressing Steel Strands in Concrete Subject to Chloride Attack, *Constr. Build. Mater.*, 2011, **25**, p 3878–3885

37. L.A. Erasmus, Cold Straightening of Partially Embedded Reinforcing Bars—A Different View, *Concr. Int.*, 1981, **3**, p 47–52

38. H. Salem and K. Maekawa, Spatially Averaged Tensile Mechanics for Cracked Concrete and Reinforcement Under Highly Inelastic Range, *J. Mater. Concr Struct Pavements/Doboku Gakkai Ronbunshu*, 1999, **42**(613), p 277–293

39. C.A. Apostolopoulos and D. Michalopoulos, The Impact of Corrosion on the Mechanical Behavior of Steel Undergoing Plastic Deformation, *Mater. Corros.*, 2007, **58**(1), p 1–12

40. X. Feng, Y. Zuo, Y. Tang, X. Zhao, and X. Lu, The Degradation of Passive Film on Carbon Steel in Concrete Pore Solution Under Compressive and Tensile Stresses, *Electrochim. Acta*, 2011, **58**, p 258–263

41. X. Feng, Y. Tang, and Y. Zuo, The Influence of Strain on the Passive Behavior of Carbon Steel in Cement Extract, *Corros. Sci.*, 2012, **65**, p 542–548

42. P.K. Behera, A.P.K. Moon, K. Mondal, and S. Misra, Estimating Critical Corrosion for Initiation of Longitudinal Cracks in RC Structures Considering Phases and Composition of Corrosion Products, *J. Mater. Civ. Eng.*, 2016, **28**(12), p 1–12

43. B. Eghbali, EBSD Study on the Formation of Fine Ferrite Grains in Plain Carbon Steel During Warm Deformation, *Mater. Lett.*, 2007, **61**, p 4006–4010

44. S. Torizuka, A. Ohmori, S.V.S.N. Murthy, and K. Nagai, Effect of Strain on the Microstructure and Mechanical Properties of Multi-Pass Warm Caliber Rolled Low Carbon Steel, *Scripta Mater.*, 2006, **54**, p 563–568

45. S. Choudhary, V. Nanda, S. Shekar, A. Garg, and K. Mondal, Effect of Microstructural Anisotropy on the Electrochemical Behavior of Rolled Mild Steel, *J. Mater. Eng. Perform.*, 2017, **26**, p 185–194

46. Specification for Mild Steel and Medium Tensile Steel Bars and Hand-Drawn Steel Wire for Concrete Reinforcement, IS: 432, Bureau of Indian Standards, Part 1, BIS, 1982, pp. 7–8

47. Metallic materials—Tensile Testing at Ambient Temperature, IS: 1608, Bureau of Indian Standards, 2005, p. 9

48. A. Poursaee and C.M. Hansson, Potential Pitfalls in Assessing Chloride-Induced Corrosion of Steel in Concrete, *Cem. Concr. Res.*, 2009, **39**, p 391–400

49. R. Balasubramaniam, A.V. Ramesh Kumar, and P. Dillmann, Characterization of Rust on Ancient Indian Iron, *Curr. Sci.*, 2003, **85**(11), p 1546–1555

50. J. Aramendia, L. Gomez-Nubla, L. Bellot-Gurlet, K. Castro, C. Paris, P. Colomban, and J.M. Madariaga, Protective Ability Index Measurement through Raman Quantification Imaging to Diagnose the Conservation state of Weathering Steel Structures, *J. Raman Spectrosc.*, 2014, **45**, p 1076–1084

51. P.K. Katiyar, P.K. Behera, S. Misra, and K. Mondal, Comparative Corrosion Behavior of Five Different Microstructures of Rebar Steels in Simulated Concrete Pore Solution with and Without Chloride Addition, *J. Mater. Eng. Perform.*, 2019, **28**, p 6275–6286

52. S. Pang, B. Diao, and Y. Ye, Effect of Sustained Load on The Passive Film of Carbon Steel Embedded in Concrete, *Int. J. Electrochem. Sci.*, 2017, **12**, p 5539–5552

53. H. Schäfer, S.M. Beladi-Mousavi, L. Walder, J. Wollschläger, O. Kuschel, S. Ichilmann, S. Sadaf, M. Steinhart, K. Küpper, and L. Schneider, Surface Oxidation of Stainless Steel: Oxygen Evolution Electrocatalysts with High Catalytic Activity, *ACS Catal.*, 2015, **5**, p 2671–2680

54. A.H. Cottrell and B.A. Bilby, Dislocation Theory of Yielding and Strain Ageing of Iron, *Proc. Phys. Soc. Section A*, 1949, **62**, p 49–62

55. C.W. Richards, *Engineering Materials Science*, 2nd ed., Chapman and Hall/Wardsworth Publishing Company, London, 1968

56. K. Karadakis, V.J. Azad, P. Ghods, and O.B. Isgor, Numerical Investigation of the Role of Mill Scale Crevices on the Corrosion Initiation of Carbon Steel Reinforcement in Concrete, *J. Electrochem. Soc.*, 2016, **163**(6), p C306–C315